# Evaluation of an Active Disturbance Rejection Controller for Ophthalmic Robots with Piezo-driven Injector

Qiannan Tao , Jianjun Liu , Yu Zheng * , Yang Yang * , Chuang Lin , Chenhan Guang

Posted Date: 11 June 2024

doi: 10.20944/preprints202406.0612.v1

Keywords: retinal vein cannulation; piezo-driven injector; ophthalmic robot; active disturbance rejection controller

 doi:10.20944/preprints202406.0612.v1



*Article*

# Evaluation of an Active Disturbance Rejection Controller for Ophthalmic Robots with Piezo-Driven Injector

**Qiannan Tao [1], Jianjun Liu [2], Yu Zheng [3,*], Yang Yang [2,*], Chuang Lin [2,†], and Chenhan Guang [4]**

[1] School of Energy and Power Engineering, Beihang University, Beijing 100191, People's Republic of China; tqn_lea@163.com
[2] School of Mechanical Engineering and Automation, Beihang University, Beijing 100191, People's Republic of China; yyds_l@vip.163.com; yang_mech@126.com; drlin@leadmicros.com
[3] College of Automation, and College of Artificial Intelligence, Nanjing University of Posts and Telecommunications, JiangSu, Nanjing, 210023, People's Republic of China.
[4] School of Mechanical and Materials Engineering, North China University of Technology, 100144, People's Republic of China. guangchenhan@ncut.edu.cn
* Correspondence: zhengyu@njupt.edu.cn; yang_mech@126.com
† Current address: Beijing Xianwei Medical Technology Co..Ltd, Beijing, 100083, People's Republic of China. drlin@leadmicros.com

**Abstract:** Retinal vein cannulation involves puncturing an occluded vessel on the micron scale. Even single millinewton force can cause permanent damage. An ophthalmic robot with a piezo-driven injector is precious enough to perform this delicate procedure, but the uncertain viscoe-lastic characteristics of the vessel makes it difficult to achieve the desired contact force without harming the retina. The paper utilizes a viscoelastic contact model to explain the mechanical characteristics of retinal blood vessels in order to tackle this issue. The uncertainty in the viscoelastic properties is considered an internal disturbance of the contact model, and an active disturbance rejection controller is then proposed to precisely control the contact force. The experimental results show that this method can precisely adjust the contact force at the millinewton level even when the viscoelastic parameters vary significantly (up to 403.8%). The root mean square (RMS) and maximum value of steady-state error are 0.32 mN and 0.41 mN. The response time below 2.51 s with no obvious overshoot.

**Keywords:** retinal vein cannulation; piezo-driven injector; ophthalmic robot; active disturbance rejection controller

## 1. Introduction

Retinal vein occlusion (RVO) occurs when a blockage of one or more small veins carries blood away from the retina. RVO has been reported to be the second most common retinal vascular occlusive disease[1]. Its impact on vision can be severe, causing blurred and distorted vision[2]. Currently, there is no available treatment to resolve RVO directly. A possible treatment is retinal vein cannulation (RVC), which involves the insertion of a cannulation needle and light pipe through the scleral ports (diameter: about 0.6mm) to inject a clot-dissolving drug into the retinal vein. Figure 1 gives a visual representation of the procedure of RVC.

Performing micro-surgical tasks in RVC requires highly specialized skills that are at the limits of human motor capabilities. The surgeons' hand tremor amplitudes exceeds 150 μm[3], which is significantly larger than the diameters of the retinal veins (50-150 μm[4]). The surgeons are not able to perceive the contact force at the needle tip, which is below 10mN[5]. The limited motor and force control, degraded manual dexterity, and possible visual, physical, and mental fatigue of a surgeon

 doi:10.20944/preprints202406.0612.v1



may intensify their hand tremors and increase the risk of sight-damaging iatrogenic trauma to the eye.

A technically feasible remedy to these challenges is robot-assisted RVC. Figure 1 illustrates the three processes involved in robot-assisted RVC: **(1) Approach** – where the robot drives the needle approaches the retinal vein. **(2) Contact – where the robot ensures that** the contact force reaches the expected value, making a puncture into the vein without causing any damage to the retina. **(3) Inject-where the robot** keeps the needle steady and injects the clot-dissolving drug into the retina vein.

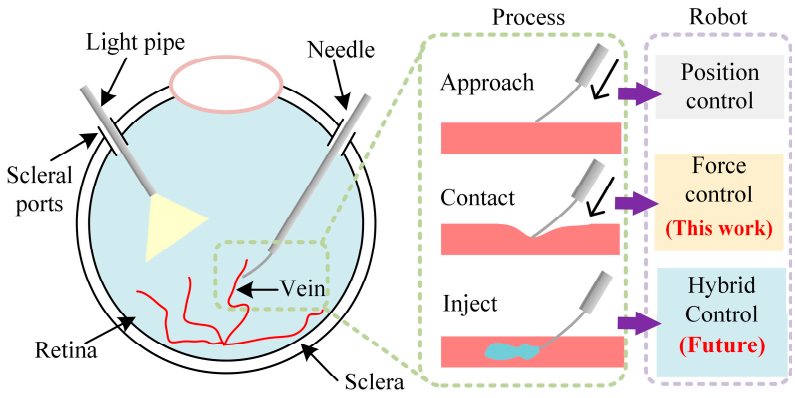


**Figure 1.** Illustration of the retinal vein canulation.

Current robots designed for robotic assisted vascular catheterization (RVC) have primarily focused on improving the precision of surgical tools and filtering out the surgeon's hand tremors. For instance, leveraging the natural steady motion of robotic arms [6–8], compensating the tool tip's motion with hand-held devices [9], wireless magnetic control of an untethered microrobot [10], localization of the tool tip with OCT[11]/computer vision [12], sensing tool-tissue proximity with bio-impedance [13]. While precise needle movement is the foundation of robot-assisted RVC, the lack of a contact force controller presents a safety challenge. A robotic system which is capable of sensing and controlling the contact force is advantageous.

Researchers from Johns Hopkins University have developed force-sensing tools that utilize fiber Bragg grating (FBG) sensors. With these sensors, the tools can measure the contact force, scleral force, and insertion depth. The force measurement can be integrated into the robot control law [14,15] or provide auditory substitution [16]. Dual force constraint controller[17], hybrid position/force controller [18] are also proposed to keep the force within desired range. In the contact process, the robot is expected to track the desired force during the contact process, not just limit the contact force.

Ebrahimi et al [19] model the sclera with linear elastic contact model and propose an adaptive controller to track the sclera force. However, the stiffness fail to describe the retina vein's viscoelastic characteristics. Additionally, the viscoelastic parameters of eye tissue are typically related to a variety of factors, such as age, gender, and species (human or different experimental animals) [20], making the contact force highly uncertain and complex. To improve the force control performance, a viscoelastic contact model and a robust controller are necessary.

The parameter uncertainty could be regarded as inner disturbance in viscoelastic contact model. Active disturbance rejection control (ADRC), presented by Han[21], is a control strategy with strong adaptability, robustness, and independence on the accurate parameters of the system model. ADRC is proved to have good rejection ability against the disturbance and noise[22,23]. To the best of our knowledge, the ADRC has not been applied to reject the inner disturbance in viscoelastic contact model and control the "needle-retina vein" contact force.

This preliminary study establishes a contact model based on viscoelastic theory to capture the nonlinear, uncertain behavior of vessel. Then, on the basis of the viscoelastic contact model, an active disturbance rejection force controller (ADRC) is designed to reject the disturbance caused by the parameter uncertainty, and precisely control the contact force. Section 2 introduces the proposed

 doi:10.20944/preprints202406.0612.v1



ophthalmic surgical robot and builds the viscoelastic contact model. Section 3 focuse on the design of the ADRC. Section 4 analyzes the disturbance rejection ability through simulation, while Section 5 presents the experimental setup and results. Section 5 concludes this paper.

## 2. Materials and Methods

### *2.1. Ophthalmic Surgical Robot*

Figure 2a and Figure 2b give the components and mechanism configuration of the ophthalmic surgical robot system, respectively. The proposed robot can perform the instruments' orientation, insertion, and rotation. The instruments' orientation are adjusted by four linear motors (LM1-4, MSR080, Paker, USA). We can rotate the instrument around or along axis $y_B$ by changing the stroke of LM1 and LM3. Similarly, we can rotate the instrument around or along axis $x_B$ by changing the stroke of LM2 and LM4. The proposed ophthalmic surgical robot can also perform continuous curvilinear capsulorhexis or membrane peeling with forceps [8,25].

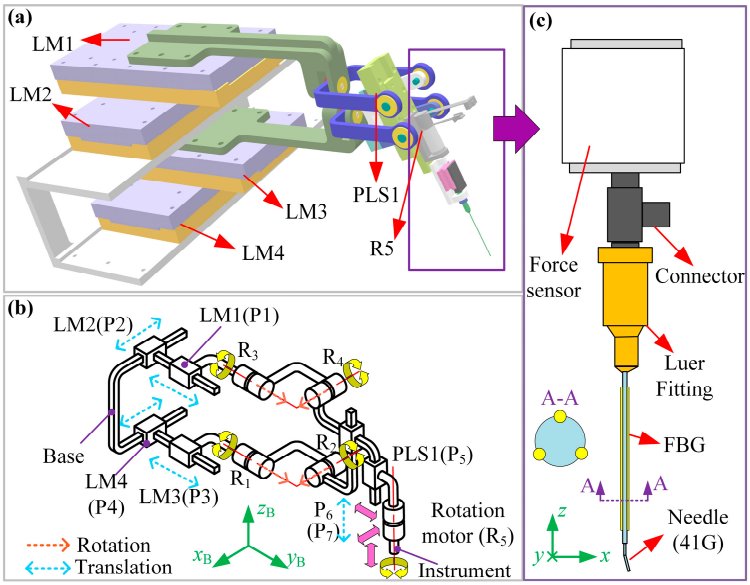


**Figure 2.** The ophthalmic robot with piezo-driven injector. (a) components. (b) configuration (c) instrument.

The piezo-driven injector consists of a piezoelectric linear stage (CONEX-SAG-LS48P, NewPort, USA, $P_5$), a rotation motor (DCX10S, Maxson, Switzerland, $R_5$) and the instrument shown in Figure 2c. The positioning accuracy of the linear motors and piezoelectric linear stage are 0.01 mm and 25 nm, respectively. The detailed components of instrument is given in Figure 2c. The instrument consists of a force sensor, a connector, a Luer fitting and a cannulation needle (41G). The needle is also equipped with three FBG sensors. The force sensor (LSB200-20g, Futek, USA, precision: 0.2 mN) aims to measure the axial force ($z$, Figure 2b-c) acting at the needle.

### *2.2. Viscoelastic Contact Model*

Figure 3 illustrates the viscoelastic contact model, which models the contact force $f(t)$ with two parallel Maxwell viscoelastic models [26]. Each Maxwell model combines a spring with a damper in serial.

Preprints.org (www.preprints.org) | NOT PEER-REVIEWED | Posted: 11 June 2024 doi:10.20944/preprints202406.0612.v1



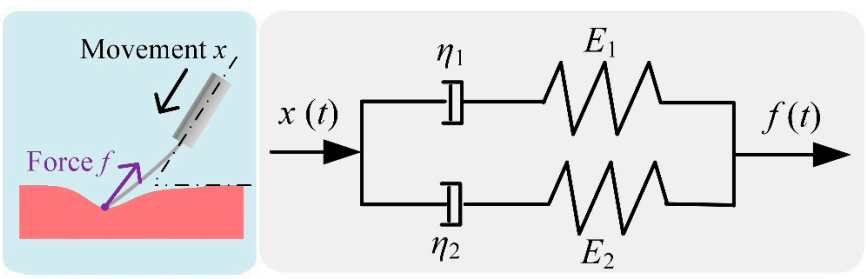


**Figure 3.** Illustration of the viscoelastic contact model.

The mathematical description of the viscoelastic contact model is given in Eq.(1).

$$f(t)=(E_1+E_2)\frac{dx(t)}{dt}-(\tau_1+\tau_2)\frac{df(t)}{dt} \tag{1}$$

where $x$(t) is the axial movement of PLS1, $\tau_i = \eta_i/E_i$, $i$=1,2. $E$ and $\eta$ represent the spring stiffness constant and the damping factor, respectively.

$E$ and $\tau$ are the mechanical parameters of the retinal vein and could be written as below:

$E = E_{ave} + \Delta E$, $\tau = \tau_{ave} + \Delta\tau$, $E=E_{ave}+\Delta E$, $\tau=\tau_{ave}+\Delta\tau$

where ave means the mean value measured by experiments, $\Delta E$ and $\Delta\tau$ are the uncertainty caused by many factors, such as age, gender, experiment models (in-vivo/ex-vivo, pig/rabbit/human),etc.

Eq.1 could be rewritten in frequency domain:

$$F(s)=\left(\frac{E_1\tau_1 s}{1+\tau_1 s}+\frac{E_2\tau_2 s}{1+\tau_2 s}\right)X(s) \tag{2}$$

where $s$ is the Laplace operator.

The step response of Eq.2 in time-domain is shown as below:

$$f(t)=E_1e^{-t/\tau_1}+E_2e^{-t/\tau_2} \tag{3}$$

Eq.3 is used to identify $E_{i,ave}$, $\tau_{i,ave}$, $i$=1,2 in contact model, which will be given in Section 5.

$\Delta E$ and $\Delta\eta$ are the main disturbance of contact model, which makes it hard to control f(t) precisely. In this paper, a LADRC-based force controller with disturbance-rejection ability is first presented and designed for viscoelastic contact model.

### *2.3. Active Disturbance Rejection Force Controller*

Figure 4 gives the block diagram of the ADRC. The ADRC consists of 3 parts: linear extended state observer (LESO), linear state error feedback (LSEF), and a numerical calculation module based on the fourth-order Runge Kutta (RK4) method. This part gives the detail design of the controller.

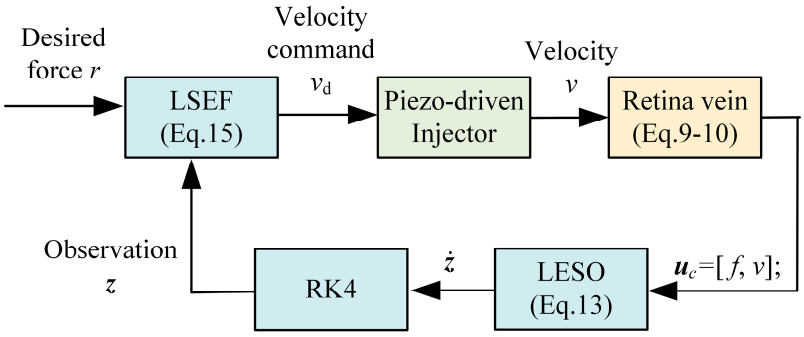


**Figure 4.** Block diagram of the ADRC.

First, we rewrite Eq.2 into Eq.4

 doi:10.20944/preprints202406.0612.v1



$$\frac{F(s)}{X(s)}=\frac{b_1 s}{1+a_1 s}+\frac{b_2 s}{1+a_2 s} \tag{4}$$

where, $\eta_i = E_i\tau_i$, $a_i=\tau_i$, $b_i=\eta_i$, $i$=1,2

Then, we can get Eq.5 by dividing $s$ on both sides of the Eq.4.

$$\frac{Y(s)}{U(s)}=\frac{F(s)}{v(s)}=\frac{b_1}{1+a_1 s}+\frac{b_2}{1+a_2 s} \tag{5}$$

where $Y(s)$ is regarded as the output of viscoelastic contact model. $v(s)$ is the velocity of the PLS1, and it is defined as the input $U(s)$.

Eq.5 could be rewritten as below:

$$\frac{Y(s)}{U(s)}=\frac{(b_1+b_2)+(a_1b_2+a_2b_1)s}{1+(a_1+a_2)s+a_1a_2s^2}=\frac{B_1s+B_2}{s^2+A_2s+A_3} \tag{6}$$

Next, we define the median parameter $Y_1(s)$ in Eq.7

$$Y_1(s)=\frac{1}{s^2+A_2s+A_3}U(s) \tag{7}$$

Submitting Eq.7 into Eq.6, we get Eq.8

$$Y(s)=Y_1(s)(B_1s+B_2) \tag{8}$$

We get Eq.9-10 by rewriting Eq.7-8 in time-domain. Eq.9 is the state equation, Eq.10 is the observation equation.

$$\begin{aligned}\ddot{y}_1 &= u-A_2\dot{y}_1-A_3y_1\\ y &= B_1\dot{y}_1+B_2y_1\end{aligned} \tag{9}$$

The uncertainty ($\triangle E$ and $\triangle\tau$) exists in both state equation and observation equation. In this paper, we only deal with the uncertainty in state equation. Then, we obtain Eq.11 by representing the uncertainty ($\triangle E$ and $\triangle\tau$) with $\omega$.

$$\begin{aligned}\ddot{y}_1 &= f+b_0u\\ y &= B_1\dot{y}_1+B_2y_1\\ f &= -A_2\dot{y}_1-A_3y_1+\omega+(1-b_0)u\end{aligned} \tag{10}$$

where $b_0$ is the known part in $u$, $f$ is the sum of uncertainty and unknown disturbance.

Next, we define the state variable $\boldsymbol{x}=\begin{bmatrix}y_1 & \dot{y}_1 & f\end{bmatrix}^{\mathrm{T}}$ and rewritte Eq.11 into Eq.12.

$$\begin{aligned}\dot{\boldsymbol{x}} &= \boldsymbol{A}\boldsymbol{x}+\boldsymbol{B}\boldsymbol{u}+\boldsymbol{E}\dot{\boldsymbol{f}}\\ \boldsymbol{y} &= \boldsymbol{C}\boldsymbol{u}\end{aligned} \tag{11}$$

where,

$$\boldsymbol{A}=\begin{bmatrix}0&1&0\\0&0&1\\0&0&0\end{bmatrix},\boldsymbol{B}=\begin{bmatrix}0\\b_0\\0\end{bmatrix},\boldsymbol{E}=\begin{bmatrix}0\\0\\1\end{bmatrix},\boldsymbol{C}=\begin{bmatrix}B_2 & B_1 & 0\end{bmatrix}$$

Then, the LESO could be obtained as below:

$$\begin{aligned}\dot{\boldsymbol{z}} &= \boldsymbol{A}\boldsymbol{z}+\boldsymbol{B}u+\boldsymbol{L}(y-\boldsymbol{C}\boldsymbol{z})\\ \hat{y} &= \boldsymbol{C}\boldsymbol{z}\end{aligned} \tag{12}$$

where $\boldsymbol{z}$ is the state variable in LESO and aims to observe $\boldsymbol{x}$.

Then, we rewritten Eq.13 into Eq.14 by ignoring the differentiation of $f$, since it could be regarded as a part of disturbance.

$$\begin{aligned}\dot{\boldsymbol{z}} &= (\boldsymbol{A}-\boldsymbol{L}\boldsymbol{C})\boldsymbol{z}+[\boldsymbol{B},\boldsymbol{L}]\boldsymbol{u}_c\\ \boldsymbol{y}_c &= \boldsymbol{z}\end{aligned} \tag{13}$$

where, $\boldsymbol{u}_c=\begin{bmatrix}u & y\end{bmatrix}^{\mathrm{T}}$, $\boldsymbol{y}_c$ is the output of the LESO.

In Eq.14, $\boldsymbol{L}$ is the gain matrix of the LESO and defined as below:

$$\boldsymbol{L}=\begin{bmatrix}3\omega_0 & 3\omega_0^2 & \omega_0^3\end{bmatrix}^T \tag{14}$$

where, $\omega_0$ is the bandwidth of the LESO.

In this paper, we solve Eq.14 with RK4. Eq.15 gives the formula of the LSEF.

 doi:10.20944/preprints202406.0612.v1



$$\begin{aligned} u_0 &= k_p\left(r - z_1\right) - k_d z_2 \\ u &= \frac{u_0 - z_3}{b_0} \end{aligned} \tag{15}$$

where $k_p = \omega_c^2, k_d = 2\omega_c$. $z_1$, $z_2$ and $z_3$ are obtained from the LESO, $\omega_c$ is the bandwidth of the LSEF, $r$ is the desired force, $u$ is the control value. $u$ is the velocity of PLS1.

## 3. Disturbance Rejection Capability Analysis

This part analyzes the disturbance-rejection capability of the proposed controller. First, we get Eq.16 by expanding Eq.13.

$$\begin{cases} \dot{z}_1 = z_2 - 3\omega_0\left(z_1 - y\right) \\ \dot{z}_2 = z_3 - 3\omega_0^2\left(z_1 - y\right) + b_0 u \\ \dot{z}_3 = -\omega_0^3\left(z_1 - y\right) \end{cases} \tag{16}$$

Then, we obtain Eq.17 by rewriting Eq.16 in frequency domain.

$$\begin{aligned} z_1 &= \frac{3\omega_0 s^2 + 3\omega_0^2 s + \omega_0^3}{\left(s + \omega_0\right)^3} y + \frac{b_0 s}{\left(s + \omega_0\right)^3} u \\ z_2 &= \frac{\left(3\omega_0^2 s + \omega_0^3\right) s}{\left(s + \omega_0\right)^3} y + \frac{b_0 s\left(s + 3\omega_0\right)}{\left(s + \omega_0\right)^3} u \\ z_3 &= \frac{\omega_0^3 s}{\left(s + \omega_0\right)^3} y - \frac{b_0 \omega_0^3}{\left(s + \omega_0\right)^3} u \end{aligned} \tag{17}$$

Submitting the LSEF into Eq.17, we get Eq.18

$$U\left(s\right) = \frac{1}{b_0} G_1\left(s\right)\left[\omega_c^2 R\left(s\right) - H\left(s\right) Y\left(s\right)\right] \tag{18}$$

where,

$$G_1\left(s\right) = \frac{\left(s + \omega_0\right)^3}{\left(s + \omega_0\right)^3 + 2\omega_c s^2 + \left(\omega_c^2 + 6\omega_c\omega_0\right) s - \omega_0^3}$$

$$H\left(s\right) = \frac{\left(3\omega_c^2\omega_0 + 6\omega_c\omega_0^2 + \omega_0^3\right) s^2 + \omega_c^2\omega_0^3}{\left(s + \omega_0\right)^3} + \frac{\left(3\omega_c^2\omega_0^2 + 2\omega_c\omega_0^3\right) s}{\left(s + \omega_0\right)^3}$$

$$Y\left(s\right) = \frac{1}{s^2}\left(B_2 + B_1 s\right)\left(f + b_0 U\right)$$

Then, we get Eq.19 by rewriting Eq.18.

$$Y\left(s\right) = D_r\left(s\right) R\left(s\right) + D_f\left(s\right) f\left(s\right) \tag{19}$$

where, $D_r(s)$ is the input sensitivity function. $D_f(s)$ is the disturbance sensitivity function. Eq.20 gives the formula of $D_f(s)$.

$$D_f\left(s\right) = \frac{k_4 s^4 + k_3 s^3 + k_2 s^2 + k_1 s}{m_5 s^5 + m_4 s^4 + m_3 s^3 + m_2 s^2 + m_1 s + m_0} \tag{20}$$

where,

$k_4 = B_1$, $k_3 = B_2 + 5B_1\omega_0$, $k_2 = 4B_1\omega_0^2 + 5B_2\omega_0 + 6B_1\omega_0\omega_c$, $k_1 = B_2\omega_0\left(4\omega_0 + 6\omega_c\right)$,

$m_5 = 1$, $m_4 = 2\omega_c + 3\omega_0$, $m_0 = B_2\omega_c^2\omega_0^3$, $m_3 = 3B_1\omega_c^2\omega_0 + \omega_c^2 + 6B_1\omega_0^2\omega_c + 6\omega_c\omega_0 + B_1\omega_0^3 + 3\omega_0^2$

$m_2 = 3B_1\omega_c^2\omega_0^2 + 3B_2\omega_c^2\omega_0 + 2B_1\omega_c\omega_0^3 + 6B_2\omega_c\omega_0^2 + B_2\omega_0^3$

$m_1 = B_1\omega_c^2\omega_0^3 + 3B_2\omega_c^2\omega_0^2 + 2B_2\omega_c\omega_0^3$

Next, we simulate the tracking performance of $D_f(s)$. All simulation are performed by MATLAB. As shown in Section 2, the disturbance comes from mechanical parameters of retinal vein. In simulation process, $\omega_c$ and $\omega_0$ are set as 16 and 60, respectively.

The range of mechanical parameters are set as below:

$E_1 \in [0.1, 2.0], E_2 \in [0.01, 10], \tau_1 \in [0.1, 2.0], \tau_2 \in [0.01, 10]$

 doi:10.20944/preprints202406.0612.v1



As shown in Figure 5, the value of $D_f(s)f(s)$ converges to zero within just one second. Changes in mechanical parameters have little effect on the simulation results. The simulation results is consistent with [22]. The proposed controller is highly resistant to disturbance.

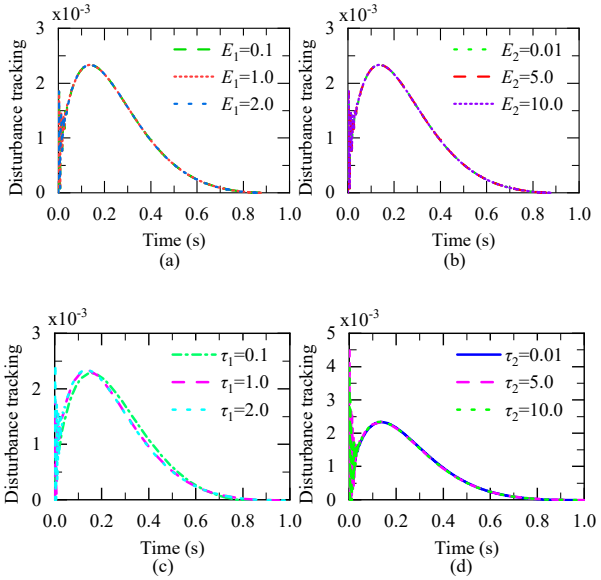


**Figure 5.** Disturbance-rejection capability of the proposed controller. (a) tracking performance of $D_f(s)$ with different $A_1$. (b) tracking performance of $D_f(s)$ with different $a_2$. (c) tracking performance of $D_f(s)$ with different $b_1$. (d) tracking performance of $D_f(s)$ with different $b_2$.

## 4. Experimental Results and Discussion

### *4.1. Experimental Setup*

Figure 6 gives the experimental setup. All experiments are performed with the proposed ophthalmic surgical robot (Section 2). A force sensor (LSB200-20g, Futek, USA, precision: 0.2 mN) and a surgical cannulation needle (41G, Incyto, South Korea, diameter: 90μm) are attached to the end of the proposed robot.

Experiments using the chicken chorioallantoic membrane of 13 days fertilized chicken embryos (Figure 7) are performed to estimate the proposed force controller. All experiments are supervised by an expert surgeon with more than 20 years clinical experience. The surgeon make sure that the cannulation needle contact the vessel precisely.

The cannulation needle is driven by the piezoelectric linear stage of the proposed robot. Data is collected using an industrial computer (ARK3523, Advantech, China), which also calculates velocity command based on ADRC and sends it to the controller of piezoelectric linear stage via USB communication. The needle's moving accuracy is approximately 25 nm. Sampling and control frequency are 200 Hz.

In this article, we perform three groups of experiments to estimate the force controller. The detail setup of each group is given as below:

**I. Parameter identification**. This group aims to identify the vein's mechanical parameter ($E_{ave}$ and $\tau_{ave}$) from step response data. In this group, the pose of robot is chosen randomly. Five embryos are used in this group. For each embryo, we adjust the robot to contact the vein, move 0.5mm along axis $z$, keep steady and record the contact force.

Preprints.org (www.preprints.org) | NOT PEER-REVIEWED | Posted: 11 June 2024 doi:10.20944/preprints202406.0612.v1



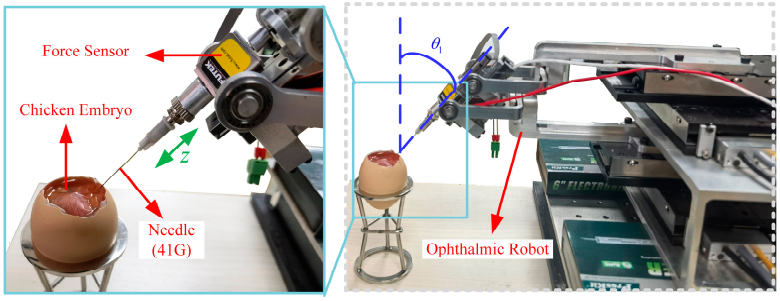


**Figure 6.** Experimental Setup.

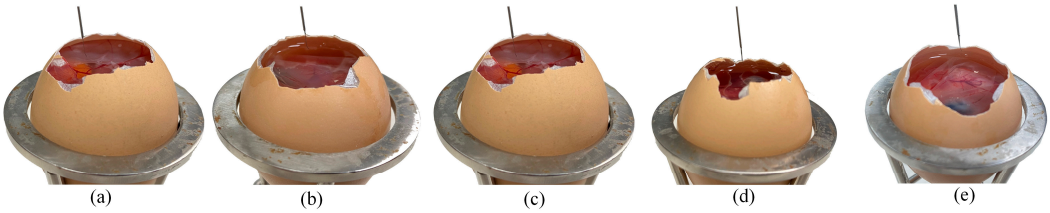


**Figure 7.** Five Tested Chicken Embryo.

For each embryo, we choose 1 contact point with 10 replicates each point. The contact point is carefully selected by an ophthalmic doctor. Then, the model parameters ($E_{i,\text{ave}}$, $\tau_{i,\text{ave}}$, $i$=1,2) in viscoelastic contact model can be obtained by fitting the collected force data to Eq.3.

**II. Step test.** This group uses another five embryos in group I. For each embryo, we adjust the robot to contact the vein, move the needle along axis z to reach the desired force. The desired force is set as 5mN. For each embryo, the pose of robot is set as 3 conditions: $\theta_1$=45°; $\theta_1$=30°; $\theta_1$=0°. For each pose, we choose 3 contact points with 5 replicates each point.

**III. Precise adjustment**. Another five embryos are used in this group. In this group, the pose of robot is same with group II.

For each pose, we choose 2 contact points with 5 replicates each point. In each test, we first set the desired force between 1mN and 5mN. Then, we increases / decreases the desired force by 1mN or 1.5 mN every 5 seconds. In Group II and Group III, after tunning, $b_0$, $\omega_c$ and $\omega_0$ are set as 20, 16 and 60, respectively.

### *4.2. Results and Discussion*

This part gives the experimental results. Figure 8 and Table 1 show the results of Group I and Group II. Figure 8(a)-(e) are the step response curve of every embryo. The fitted parameters ($E_{i,\text{ave}}$, $\tau_{i,\text{ave}}$, $i$=1,2) are given in Table 1. Figure 8(f)-(j) are the results of Group II.

The steady state error (SSE) and response time are also given in Table 1. As shown in Figure 8 and Table 1, for all tested embryos, the coefficient of determination $R^2$ is over 0.97. That means all the fitted parameters are reliable. But the value of $E_{1,\text{ave}}$, $\tau_{1,\text{ave}}$, $E_{2,\text{ave}}$, $\tau_{2,\text{ave}}$ reach variation of over 81.2%, 73.4%, 403.8%, 172.3%, respectively. The model parameters do show large interindividual differences. With the proposed controller, the SSE is [0.24, 0.35] mN. The response time ranges from 1.41s to 2.23s. No obvious overshot occurs. The proposed controller is capable of rejecting the disturbance caused by the uncertainty of contact model.

 doi:10.20944/preprints202406.0612.v1



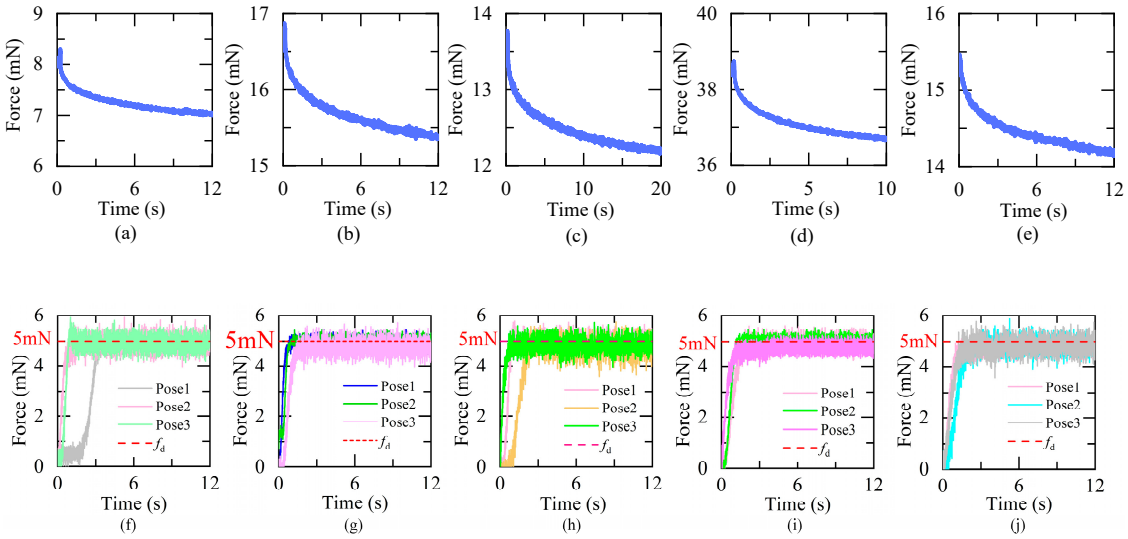


**Figure 8.** Experimental results of Group I and Group II. (a)-(e) Force release curve of each embryo. (f)-(j) Step response of Group II.

**Table 1.** Experimental results of Group I and Group II.

| | Group I | | | | | Group II | |
|---|---|---|---|---|---|---|---|
| | $E_1$ | $\tau_1$ | $E_2$ | $\tau_2$ | $R^2$ | *SSE* (mN) | *Response time*(s) |
| Embryo1 | 0.692 | 1.042 | 7.405 | 0.004611 | 0.9789 | 0.31 | 1.41 |
| Embryo2 | 0.7765 | 1.038 | 15.865 | 0.00272 | 0.9834 | 0.29 | 1.93 |
| Embryo 3 | 0.801 | 0.6156 | 12.665 | 0.002042 | 0.9812 | 0.35 | 1.97 |
| Embryo 4 | 1.254 | 1.068 | 37.31 | 0.001693 | 0.9735 | 0.24 | 1.80 |
| Embryo 5 | 0.701 | 0.9863 | 14.62 | 0.002621 | 0.9881 | 0.32 | 2.23 |

As shown in Figure 9(a)-(e), the proposed controller can adjust the contact force at 1-mN interval. No obvious overshot occurs in Group III. The root mean square (RMS) value of SSE of Group II and Group III are 0.25mN, and 0.41mN, respectively. The response time ranges from 1.04s to 2.51s, the RMS and maximum SSE are 0.32 mN and 0.47 mN, respectively.

Experimental results indicate the proposed ADRC controller is capable of rejecting the disturbance and controlling the contact force precisely. The RMS value of SSE is lower than the acceptable overshot in previous works (0.9 mN) [15,17], close to the force sensing accuracy in previous work (about 0.3 mN) [7,14,18]. In Group III, the larger error associated with "decreasing the desired force" might be attributed to the hysteresis influence of vein.

About 80% of the vein puncture force is less than 5mN[5]. Hence, the same value is adopted as the desired force in Group II. The standard deviation of vein puncture force is 1mN[5]. Therefore, the same value is set as the force intervals.

In this article, the contact force is measured by a commercial force sensor, which is too large to enter the scleral port. This issue could be relieved by replacing the force sensor with customized micro-force sensor developed by FBG, which is a part of our ongoing study. The force sensor's precision (0.2 mN) is higher than FBG force sensors (2 mN[27]). As a result, we believe the measured force data is reliable, and the proposed controller is suitable for retina vein cannulation.

 doi:10.20944/preprints202406.0612.v1



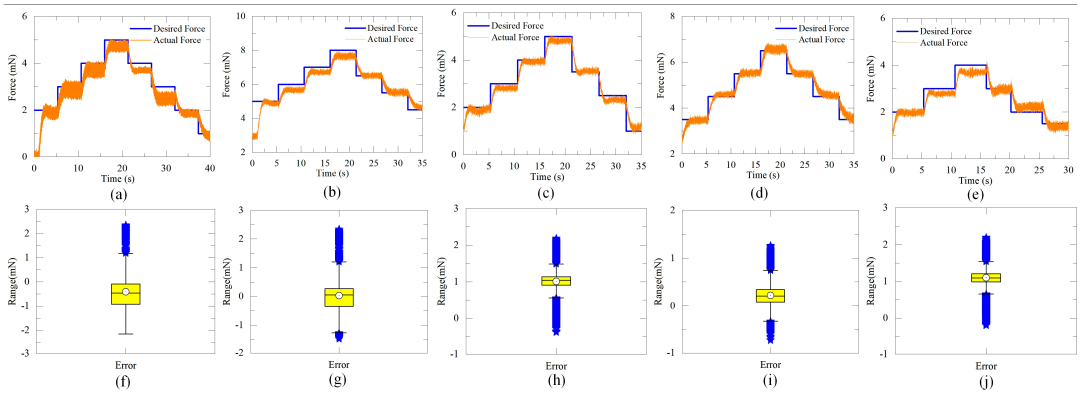


**Figure 9.** Experimental results and error of Group III. (a)-(e) force response of five embryos. (f)-(j) force error of five embryos.

It is possible to reduce the response time by increasing $\omega_c$,but this can result in severe overshot, which increase surgical risk. Therefore, we choose to prioritize reducing the overshot, even if it means sacrificing response time.

We did not perform dynamic tracking experiments for the following reason. The proposed controller aims to reject disturbance and control the force during the contact process shown in Figure 1. The expected force should precisely puncture the vein without damaging retina. In this context, the expected force is more likely to be static and specific, rather than dynamic. Therefore, we choose to perform step response experiment and precise adjustment experiment to evaluate the disturbance rejection ability of the ADRC.

While dynamic force might have potential benefits in RVC, this paper focuses on the disturbance rejection ability of the proposed controller. The effect of dynamic force, validating this work with more samples (in-vivo/ex-vivo, pig/rabbit) belong to our ongoing study.

In our study, we use two sets of embryos, which we refer to as Group I and Group II. The reason for this is that in experimental studies, we are able to collect data and identify the viscoelastic contact model multiple times. However, in clinical settings, the parameters of each tested sample can vary significantly from the identified model, resulting in increased control error.

Our proposed method is able to accurately identify the precise value of each tested sample based on previously collected data, allowing us to control the contact force with great precision. This precise control of the contact force is the key feature of our proposed method.

The embryos in Group I are used to collect data, while the embryos in Group II are the samples tested in the clinical setting. By using the data collected from Group I, our proposed method is able to accurately control the contact force in Group II, even though the embryos in Group II are completely different from those in Group I. For this work, the ADRC is designed such that the robot can control the contact force automatically. In the future, a hybrid control method will be investigated for injecting clot-dissolving drugs, which will simultaneously limit the needle's position and contact force. This could be a potential solution to free surgeons from extremely difficult injection procedures and improve overall surgical efficiency.

## 5. Conclusion

This preliminary study presents an ADRC to reject the disturbance caused by vessel's uncertain viscoelastic characteristic, and control the "needle-vessel" contact force precisely. We first model the nonlinear, uncertain behavior of the vessel with a viscoelastic contact model. Then, an ADRC is proposed based on the viscoelastic contact model. Fertilized chicken embryos are used to identify the viscoelastic model, and estimate the ADRC. Results show that ADRC can precisely control the contact force when viscoelastic parameters changes greatly. The contact force can be adjusted at 1mN interval. The RMS and maximum value of SSE are 0.32 mN and 0.41 mN, respectively. No obvious

 doi:10.20944/preprints202406.0612.v1



overshot occurs during experiments. This study provides a potential way to perform technically difficult RVC procedures.

**Author Contributions:** Conceptualisation, Q.N.T and Y. Z.; Data curation and validation, Y. Z., J.J.Liu. and C. Lin; writing-original draft preparation, Q.N.T and Y. Z.; writing-review and editing, Y. Z. and C. H. Guang; Supervision, Y. Y. All authors have read and agreed to the published version of the manuscript.

**Informed Consent Statement:** Informed consent was obtained from all subjects involved in this study.

**Data Availability Statement:** Data is contained within the article or supplementary material.

**Acknowledgments:** This work was supported in part by the Natural Science Foundation of Jiangsu Province of China (No. BK20230366), the Natural Science Research Start-Up Foundation of Recruiting Talents of Nanjing University of Posts and Telecommunications (No. NY223044), the National Natural Science Foundation of China (No. 51785011, 52205002), the National Key R&D Program of China (No. 2017YFB1302702)

**Conflicts of Interest:** The authors declare no conflicts of interest.

## References

1. Rehak, J.; Rehak, M. Branch retinal vein occlusion: Pathogenesis, visual prognosis, and treatment modalities. *Current Eye Res*. **2008**, 33(2), 111-131.
2. Wong, T. Y.; Scott, I. U., Retinal-vein occlusion. *New England J. Med*. **2010**, 363(2), 2135-2144.
3. Zheng,Y.; Yang, X. H.; Mo, B.; Qi, Y.; Yang, Y.; Lin, C.; Han, S. F.; Wang, N. L.; Guang, C. H.; Liu, W. Evaluation of the Hand Motion and Peeling Force in Inner Limiting Membrane Peeling. *Transl. Vis. Sci. Technol.* **2023**, 12(32), 1-10.
4. Bynoe, L. A.; Hutchins, R. K.; Lazarus, H. S.; Friedberg, M. A. Retinal endovascular surgery for central retinal vein occlusion: Initial experience of four surgeons. *Retina.* **2005**, 25(5), 625-632.
5. Poorten, E. V.; Riviere, C. N.; Abbott, J. J.; Bergeles, C.; Nasseri, M. A.; Kang, J. U.; Sznitman, R.; Faridpooya, K.; Iordachita, I. *Physiologicalbook of Robotic and Image-Guided Surgery-Part 36: Robotic Retinal Surgery;* Elsevier: Netherlands, 2020.
6. Zhou, M. C.; Yu, Q. M.; Huang, K.; Mahov, S.; Eslami, A.; Maier, M.; Lohmann, C. P.; Navab, N.; Zapp, D.; Knoll, A.; Nasseri, M. A. Towards Robotic-Assisted Subretinal Injection: A Hybrid Parallel-Serial Robot System Design and Preliminary Evaluation. *IEEE Trans. Ind. Electron.* **2024**, 67(8), 6617-6628.
7. He, C. Y.; Yang, E.; Patel, N.; Ebrahimi, A.; Shahbazi, M.; Gehlbach, P.; Iordachita, I. Automatic Light Pipe Actuating System for Bimanual Robot-Assisted Retinal Surgery. *IEEE-ASME Trans. Mechatron.* **2020**, 25(6), 2846-2857.
8. Zheng, Y.; Yang, Y.; Lin, C.; Guang, C. H.; Zong, J. J.; Ma, K. Preliminary Estimation of the Friction between Force-sensing Forceps and Cornea. In Proceedings of IEEE RAS-EMBS International Conference on Biomedical Robotics and Biomechatronics (BioRob), Seoul, Korea, Republic of, 21-24 August 2022, 1-6.
9. Yang, S.; MacLachlan, R. A.; Martel, J. N., Lobes, L. A.; Riviere, C. N. Comparative Evaluation of Handheld Robot-Aided Intraocular Laser Surgery. *IEEE Trans. Robot*. **2016**, 32(1), 246-251.
10. Charreyron, S. L.; Boehler, Q.; Danun, A. N.; Mesot, A.; Becker, M.; Nelson, B. J. A Magnetically Navigated Microcannula for Subretinal Injections. *IEEE Trans. Biomed. Eng.* **2021**, 68(1), 119-129.
11. Keller, B.; Draelos, M.; Zhou, K.; Qian, R. B.; A. Konidaris, N. G.; Hauser, K.; Izatt, J. A. Optical Coherence Tomography-Guided Robotic Ophthalmic Microsurgery via Reinforcement Learning from Demonstration. *IEEE Trans. Robot.* **2020**, 36(4), 1207-1218.
12. Zhou, M. C.; Hao, X.; Eslami, A.; Huang, K.; Cai, C. X.; Lohmann, C. P.; Navab, N.; Knoll, A.; Nasseri, M. A. 6DOF Needle Pose Estimation for Robot-Assisted Vitreoretinal Surgery. *IEEE Access.* **2019**, 7, 63113-63122.
13. Schoevaerdts, L.; Esteveny, L.; Gijbels, A.; Smits, J.; Reynaerts, D.; Vander Poorten, E. Design and evaluation of a new bioelectrical impedance sensor for micro-surgery: application to retinal vein cannulation. *Int. J. Comput. Assist. Radiol. Surg.* **2019,** 14(2), 311-320.
14. Ebrahimi, A.; Urias, M. G.; Patel, N.; Taylor, R. H.; Gehlbach, P., Iordachita, I. Adaptive control improves sclera force safety in robot-assisted eye surgery: A clinical study. *IEEE Trans. Biomed. Eng.* **2021**, 68(1), 3356-3365.

 doi:10.20944/preprints202406.0612.v1




15. He, C. Y.; Patel, N.; Shahbazi, M.; Yang, Y.; Gehlbach, P.; Kobilarov, M.; Iordachita, I. Toward Safe Retinal Microsurgery: Development and Evaluation of an RNN-Based Active Interventional Control Framework. *IEEE Trans. Biomed. Eng.* **2020**, 67(4), 966-977.
16. He, C. Y.; Patel, N.; Iordachita, I.; Kobilarov, M. Enabling Technology for Safe Robot-Assisted Retinal Surgery: Early Warning for Unsafe Scleral Force. In Proceedings of the IEEE International Conference on Robotics and Automation (ICRA), Montreal, QC, Canada, 20-24 May 2019, 3889-3894.
17. He, C. Y.; Ebrahimi, A.; Yang, E.; Urias, M.; Yang, Y.; Gehlbach, P.; Iordachita, I. Towards Bimanual Vein Cannulation: Preliminary Study of a Bimanual Robotic System With a Dual Force Constraint Controller. In Proceedings of the IEEE International Conference on Robotics and Automation (ICRA), Paris, France, 31 May 2020 - 31 August 2020, 4441-4447.
18. Wells, T. S.; Yang, S.; MacLachlan, R. A.; Lobes, L. A.; Martel, J. N.; Riviere, C. N. Hybrid position/force control of an active handheld micromanipulator for membrane peeling. *Int. J. Med. Robot. Comput. Assist. Surg.*, **2016**, 12(1), 85-95.
19. Ebrahimi, A.; Patel, N.; He, C. Y.; Gehlbach, P.; Kobilarov, M.; Iordachita, I. Adaptive Control of Sclera Force and Insertion Depth for Safe Robot-Assisted Retinal Surgery. In Proceedings of the IEEE International Conference on Robotics and Automation (ICRA), Montreal, QC, Canada, 20-24 May 2019, 9073-9079.
20. Avetisov, K. S.; Bakhchieva, N. A.; Avetisov, S. E.; Novikov, I. A.; Frolova, A. A.; Akovantseva, A. A.; Efremov, Y. M.; Kotova, S. L.; Timashev, P. S. Biomechanical properties of the lens capsule: A review. *J. Mech. Behav. Biomed. Mater.* **2020**, 103, 103600.
21. Han, J. From PID to active disturbance rejection control. *IEEE Trans. Ind. Electron.* **2009**, 56(3), 900-906.
22. Liu, H.; Bu, F.; Huang, W.; Qin, H.; Tan, Y.; Qian, Z. Linear active disturbance rejection control for dual-stator winding induction generator AC power system. *IEEE Trans. Ind. Electron.* **2022**, 70(7), 6597-6607.
23. Zhou, R.; Fu, C.; Tan, W. Implementation of linear controllers via active disturbance rejection control structure. *IEEE Trans. Ind. Electron.* **2020**, 68(7), 6217-6226.
24. Smits, J.; Reynaerts, D.; Vander Poorten, E. Synthesis and methodology for optimal design of a parallel remote center of motion mechanism: Application to robotic eye surgery. *Mech. Mach. Theory.* **2020**, 151, 103896.
25. Lin, C.; Guang, C. H.; Zheng, Y.; Ma, K.; Yang, Y. Preliminary evaluation of a novel vision-guided hybrid robot system for capsulotomy in cataract surgery. *Displays*. **2022**, 74, 102262.
26. Moreira, P.; Zemiti, N.; Liu, C.; Poignet, P. Viscoelastic model based force control for soft tissue interaction and its application in physiological motion compensation. *Comput. Meth. Programs Biomed.* **2014**, 116(2), 52-67.
27. Gonenc, B.; Chamani, A.; Handa, J.; Gehlbach, P.; Taylor, R. H.; Iordachita, I. 3-DOF Force-Sensing Motorized Micro-Forceps for Robot-Assisted Vitreoretinal Surgery. *IEEE Sens. J.* **2017**, 17(11), 3526-3541.